

A semester project conducted at the  
PAUL SCHERRER INSTITUTE  
on the

---

## Setup and Characterization of a 4-bore tunable cavity

---

by ETIENNE CORMINBOEUF  
under supervision by  
DR. CORNELIUS HEMPEL and PROF. JONATHAN HOME in  
Zurich, 30th November 2022.

## Table of Contents

1	INTRODUCTION	1
2	THEORY	2
2.1	Cavity . . . . .	3
2.2	Pound-Drever-Hall Lock . . . . .	6
3	SETUP	10
3.1	Optical Setup . . . . .	10
3.2	4-bore tunable cavity . . . . .	11
4	CHARACTERIZATION AND INTERPRETATION	13
4.1	Tuning Range Calibration . . . . .	13
4.2	Settling after Tuning . . . . .	15
4.3	Hysteresis . . . . .	17
4.4	Longterm Drift . . . . .	19
5	SUMMARY AND OUTLOOK	23
6	ACKNOWLEDGEMENTS	24

# 1 Introduction

Trapped ions are a promising platforms for quantum computation and simulation, due to the long coherence times of the qubits implemented therein and the ability to do high-fidelity measurements and state readout [1]. Current systems are of the size of tens of qubits but multiple approaches are currently being investigated to scale trapped ion quantum processors such as the long string [2] and QCCD [3] architecture. For trapped ion quantum computation most often earth-alkali atomic ions - such as Beryllium, Calcium and Strontium - are used because of their simple electronic structure. Methods commonly employed to trap these ions are the Paul trap - where static and oscillating RF electric fields are used to create an effective trapping potential - and the Penning trap - where the ions are constrained by a static electric field and a strong static magnetic field. [4]

State preparation, transitions and readout in trapped ions are often implemented via laser beams driving optical transitions between different logical and auxiliary states. To avoid introducing decoherence into the system the drive frequency should be well stabilized to the transition, which can be achieved by using an external reference cavity and the Pound-Drever-Hall locking scheme [5].

In this paper we describe the efforts undertaken to implement frequency stabilization of a laser to a tunable cavity with low finesse and characterize the piezo actuators built into said cavity. In Section 2 we introduce the necessary theoretical foundations on frequency stabilization using cavities and the locking procedure. In Section 3 we describe the setup built to implement frequency locking and describe the cavity. In Section 4 we show the experiments we conducted using the cavity: in Section 4.1 we determine the tuning range calibration that relates the voltage differences that we apply to the frequency displacement this causes. In Section 4.2 we describe the settling behaviour after tuning, in Section 4.3 we characterize the hysteresis of the piezo actuators and in Section 4.4 we analyze the longterm stability of a laser stabilized to the cavity. Finally in Section 5 we summarize our findings and give an outlook.

## 2 Theory

The techniques discussed in this paper are related to an experiment working with  $^{40}\text{Ca}^+$ , thus we will briefly explain their relevance based on that example. In  $^{40}\text{Ca}^+$ , state-preparation, state-transitions and readout are implemented using laser beams driving optical transitions. The energy level structure of  $^{40}\text{Ca}^+$  for an external magnetic field of 119 G is visible in Figure 2.1.

Usually the  $S_{1/2}$  state is used as the logical  $|0\rangle$  state, the  $D_{5/2}$  as the logical  $|1\rangle$  state.

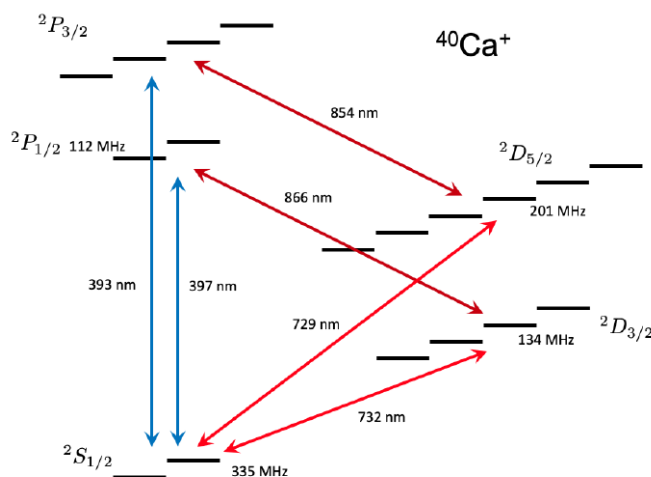


Figure 2.1: Energy level structure of  $^{40}\text{Ca}^+$  with an external magnetic field of 119 G. Usually the  $S_{1/2}$  state is used as the logical  $|0\rangle$ , the  $D_{5/2}$  as the logical  $|1\rangle$ . The  $S_{1/2} \leftrightarrow P_{1/2}$  transition is a good cycling transition, thus  $P_{1/2}$  is used for readout. The  $P_{3/2}$  and  $D_{3/2}$  levels are relevant for repumping. The 732 nm and 393 nm transitions are dipole transitions that do not have a dedicated laser in our lab. Figure taken from [4].

The 854 nm, 866 nm and 397 nm transitions are dipole transitions, the first two being used for qubit reset and repumping and the latter for readout. The 397 nm transition has a linewidth of around 22.4 MHz. Additionally a 423 nm transition is used for photo-ionization. The 729 nm transition is a quadrupole transition and is used for qubit manipulation. A laser driving one of the aforementioned transitions should be well stabilized to the respective frequency to avoid introducing decoherence into the system. For the 729 nm quadrupole transition - which has a very small linewidth of 130 mHz - we have strict stability requirements as the laser linewidth needs to be smaller than the transition linewidth [4].

The internal stabilization of a commercial laser is not sufficient for our applications. We achieve the requirements by stabilizing the laser frequency to an external reference cavity.

## 2.1 Cavity

Before talking about cavities, we must quickly introduce the notion of Gaussian beams. We follow the derivation in [6, 7].

Electromagnetic waves in a uniform and isotropic medium are governed by the wave equation

$$\left(\nabla^2 - \frac{1}{c^2} \frac{\partial^2}{\partial t^2}\right) u(\mathbf{r}, t) = 0. \quad (2.1)$$

Assuming that the solution is separable -  $u(\mathbf{r}, t) = \tilde{u}(\mathbf{r})\phi(t)$  - the spatial part reduces to the paraxial wave equation (or Helmholtz equation)

$$[\nabla^2 + k^2]\tilde{u}(x, y, z) = 0. \quad (2.2)$$

Solutions to this equation are of the form

$$\tilde{u}(x, y, z) = \frac{1}{\tilde{q}(z)} \exp\left(-ik \frac{x^2 + y^2}{2R(z)} - \frac{x^2 + y^2}{\omega^2(z)}\right) \quad (2.3)$$

where  $R(z)$  is the radius of curvature,  $\omega(z)$  the beam radius and  $\tilde{q}(z)$  the complex radius. These three quantities are defined through

$$\omega(z) = \omega_0 \sqrt{1 + \left(\frac{z}{z_R}\right)^2} \quad (2.4)$$

$$R(z) = z + \frac{z_R^2}{z} \quad (2.5)$$

$$\tilde{q}^{-1}(z) = R^{-1}(z) - i \frac{\lambda}{\pi \omega^2(z)}, \quad (2.6)$$

where  $\omega_0$  is the initial beam waist,  $z_R = \pi \omega_0^2 / \lambda$  is the Rayleigh length and  $\lambda$  the wavelength. Electromagnetic waves of this form are called Gaussian beams.

A Fabry-Perot cavity is comprised of a set of two mirrors at a distance  $L$ . The shape of the mirrors depends on the application. If the radius of curvature  $R(z)$  of a Gaussian beam matches each mirrors curvature at the respective mirrors location then this Gaussian beam can build up a standing wave inside the cavity. We will call this Gaussian mode *resonant* with the cavity. A cavity can often not only support a single Gaussian mode but also higher order Hermite-Gauss or Laguerre-Gauss modes.

Important parameters to characterize cavities are the radius of curvature  $R_1$ ,  $R_2$  of the mirrors ,where 1 (2) refers to first (second) mirror, and the g-parameters, which are defined as

$$g_{1,2} = 1 - \frac{L}{R_{1,2}}. \quad (2.7)$$

We can express the beam waist introduced in Equation (2.4) in terms of the g-factors

$$\omega_0^2 = \frac{L\lambda}{\pi} \sqrt{\frac{g_1 g_2 (1 - g_1 g_2)}{(g_1 + g_2 - 2g_1 g_2)}}. \quad (2.8)$$

The beam waist at the position of the two mirrors

$$\omega_1^2 = \frac{L\lambda}{\pi} \sqrt{\frac{g_2}{g_1(1 - g_1 g_2)}} \quad (2.9)$$

$$\omega_2^2 = \frac{L\lambda}{\pi} \sqrt{\frac{g_1}{g_2(1 - g_1 g_2)}} \quad (2.10)$$

is of particular importance, as it allows us to derive a stability criterion: Two mirrors with radii  $R_1$ ,  $R_2$  respectively give rise to a stable solution only if

$$0 \leq g_1 g_2 \leq 1. \quad (2.11)$$

The cavity mirrors are also characterized by their reflection and transmission coefficients  $r$ ,  $t$ . Light that is fed into the cavity is reflected with a factor of  $r$  and transmitted with a factor of  $t$ , where  $t$ ,  $r$  are related via

$$r^2 + t^2 = 1, \quad 0 \leq r, t \leq 1. \quad (2.12)$$

This is equivalent to stating that no power is lost in the process, e.g. through absorption in the mirrors. Assuming an incoming electrical field  $E_i = E_0 e^{i\omega t}$ , the field reflected off the first mirror is then  $E_r = rE_i$  and the field transmitted beyond the first mirror is  $E_t = tE_i$ . The field reflected off the first mirror is not the only contribution to the total reflected field. Rather, we need to consider leakage from the cavity as well. The leakage field is comprised of all the contributions of light that is transmitted into the cavity, reflected off the internal mirrors and then at some point transmitted through mirror 1. An illustration is visible in Figure 2.2.

Light reflected directly off the first mirror picks up a phase of  $\pi$ . Alternatively, in a full round trip within the cavity the light acquires a phase of  $\phi = \omega T_\phi = 2\pi \cdot 2L/\lambda$  [8]. Thus the total reflected field is

$$E_r = E_i(r_1 e^{i\pi} + t_1 r_2 t_1 e^{i\phi} + t_1 r_2 r_1 r_2 t_1 e^{i2\phi} + \dots) \quad (2.13)$$

$$= E_i(-r_1 + \frac{t_1^2 r_2 e^{i\phi}}{1 - r_1 r_2 e^{i\phi}}), \quad (2.14)$$

where we used the geometric series identity  $\sum_{i=0}^{\infty} q^i = \frac{1}{1-q}$ .

The reflectivity of a cavity  $F(\omega)$ , which we will later use in Section 2.2 to derive the error signal for the Pound-Drever-Hall lock, is then

$$F(\omega) = \frac{E_r}{E_i} = -r_1 + \frac{t_1^2 r_2 e^{i\phi}}{1 - r_1 r_2 e^{i\phi}}. \quad (2.15)$$

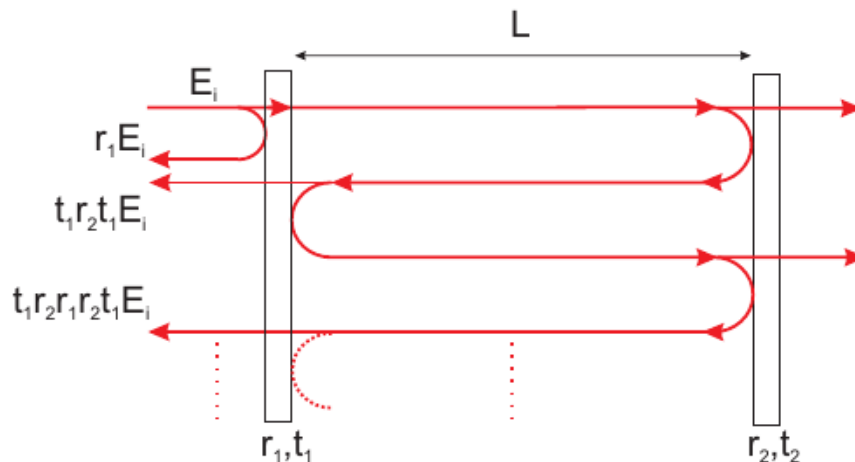


Figure 2.2: Illustration of the terms that make up the leakage field out of mirror 1, shown in Equation (2.13). Graphic was taken from [8].

We additionally introduce two important quantities for a cavity: The free spectral range, FSR and the finesse,  $\mathcal{F}$ . The *FSR* denotes the frequency separation of two  $\text{TEM}_{00}$  modes and is defined as

$$\text{FSR} = \frac{c}{2L}, \quad (2.16)$$

where  $c$  is the speed of light and  $L$  the cavity length. The finesse  $\mathcal{F}$  is a measure for the average time a photon transmitted into the cavity remains in the cavity and is defined as

$$\mathcal{F} = \frac{\pi\sqrt{g_{rt}}}{1 - g_{rt}}, \quad (2.17)$$

where  $g_{rt}$  is the round-trip gain (the probability for a photon to remain in the cavity per round-trip). Accounting for photon loss - i.e. through absorption in the mirrors or scattering in the path - with probability  $l$ ,  $g_{rt} = lr_1r_2$ .  $\mathcal{F}$  also corresponds to the ratio of the FSR and the cavity bandwidth  $\Delta\nu$ . From this relation it becomes apparent that increasing the cavity finesse e.g. through reducing losses and increasing reflectivity reduces the cavity linewidth.

We can use the FSR and  $\mathcal{F}$  as defined above to simplify the expression in Equation (2.13). For a symmetric cavity (with  $r_1 = r_2$ ) it can be converted into

$$E_r = -E_i r \frac{e^{i\frac{\omega}{\text{FSR}}} - 1}{1 - r^2 e^{i\frac{\omega}{\text{FSR}}}}. \quad (2.18)$$

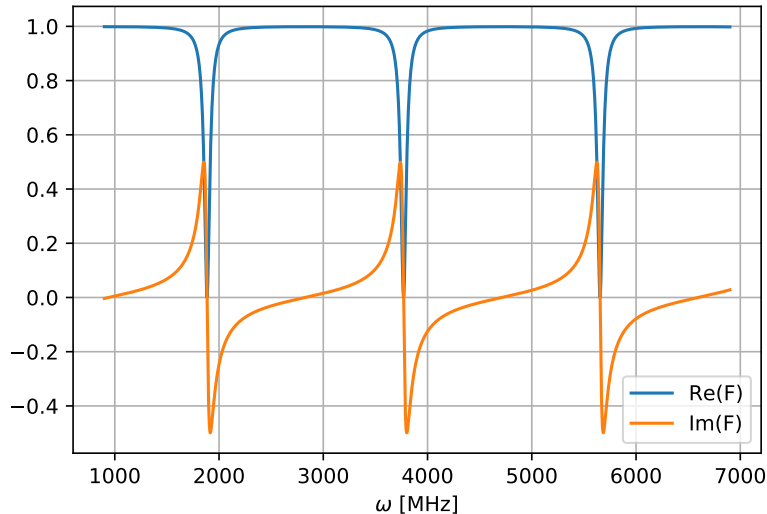


Figure 2.3: Plot of the reflectivity of a symmetric cavity ( $r_1 = r_2$ ) for example parameters  $L = 0.5m$ ,  $r = 0.95$  and consequentially  $t = \sqrt{1 - r^2} \approx 0.31$ . On resonance the real part  $\text{Re}(F)$  vanishes whereas the imaginary part  $\text{Im}(F)$  has a zero crossing. The fact that  $\text{Im}(F)$  is antisymmetric around resonance is vital for the PDH lock, as it contains information both about the direction and magnitude of displacement from resonance.

## 2.2 Pound-Drever-Hall Lock

For many applications the stability of a lasers frequency as given by the laser itself is not sufficient. One possibility is to lock the laser to a stable reference cavity where the desired laser frequency is resonant with the cavity.

A frequently used technique for laser frequency stabilization is the so called *Pound-Drever-Hall Lock* (PDH) which was introduced by Drever and Hall in 1983. [9]. In the PDH scheme an electro-optic modulator (EOM) is introduced into the laser path and used to modulate the laser signal. The modulated signal is then fed to the cavity. Its reflection is collected at a photodiode (PD) and mixed with the RF modulation signal to create an error signal which is highly sensitive to frequency deviations from the cavity resonance. This information is then fed back to the laser and used to bring it back to the desired frequency.

The PDH locking scheme has the benefit of being both fast (faster than the cavity response time) and being able to distinguish intensity from frequency fluctuations. The introduction to PDH locking below follows [5] and [10].

A simplified sketch of the setup necessary for PDH locking is visible in Figure 2.4.

A laser signal with vertical polarization is fed into an EOM which is driven by a RF source at a frequency  $\Omega$ . The output signal consists of a carrier signal at  $\omega$  and two sidebands at  $\Omega \pm \omega$ . The light passes through a polarizing beam splitter (PBS) and a quarter-wave plate which rotates the polarization from vertical to right-polarized. In

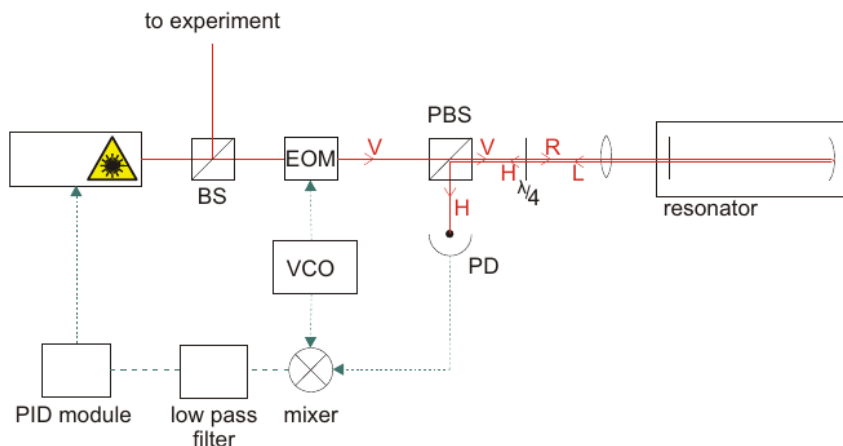


Figure 2.4: Simplified setup sketch, taken from [11]. The red markings denote the polarization, H for horizontal, V for vertical, R for right-polarized, L for left-polarized.

the cavity the reflected light acquires a  $\pi$  phase shift. The now left-polarized light is converted into horizontal polarization at the second pass of the  $\lambda/4$  wave plate and thus fully reflected at the PBS. The PD measures the incident light and outputs signals at the beat notes between carrier and sidebands. This electrical signal is then mixed with the RF driving signal, passes through a low-pass filter and is fed into a PID loop which in turn is used to control the laser frequency at the laser module.

We will now formalize this. The light incident to the EOM can be described by

$$E = E_0 e^{i\omega t}. \quad (2.19)$$

The EOM modulates this field at a modulation frequency  $\Omega$ , thus the field incident to the cavity is

$$E_{inc} = E_0 e^{i(\omega t + \beta \sin(\Omega t))} \quad (2.20)$$

$$\approx [J_0(\beta) + 2iJ_1(\beta) \sin(\Omega t)] e^{i\omega t} \quad (2.21)$$

$$= E_0 [J_0(\beta) e^{i\omega t} + J_1(\beta) e^{i(\omega + \Omega)t} - J_1(\beta) e^{i(\omega - \Omega)t}] \quad (2.22)$$

where we introduced the modulation depth  $\beta$ , directly rewrote the expression using the Bessel functions of zeroth and first order,  $J_0$  and  $J_1$  and neglected higher-order terms. This is a good approximation for small  $\beta$ . The power of the incident signal is given as  $P_0 = |E_0|^2$ . We identify the power in the carrier  $P_c = J_0^2(\beta)P_0$  and in the first-order sidebands  $P_s = J_1^2(\beta)P_0$ .

The field that is reflected from the cavity is given by

$$E_{ref} = E_0 [F(\omega) J_0(\beta) e^{i\omega t} + F(\omega + \Omega) J_1(\beta) e^{i(\omega + \Omega)t} - F(\omega - \Omega) J_1(\beta) e^{i(\omega - \Omega)t}] \quad (2.23)$$

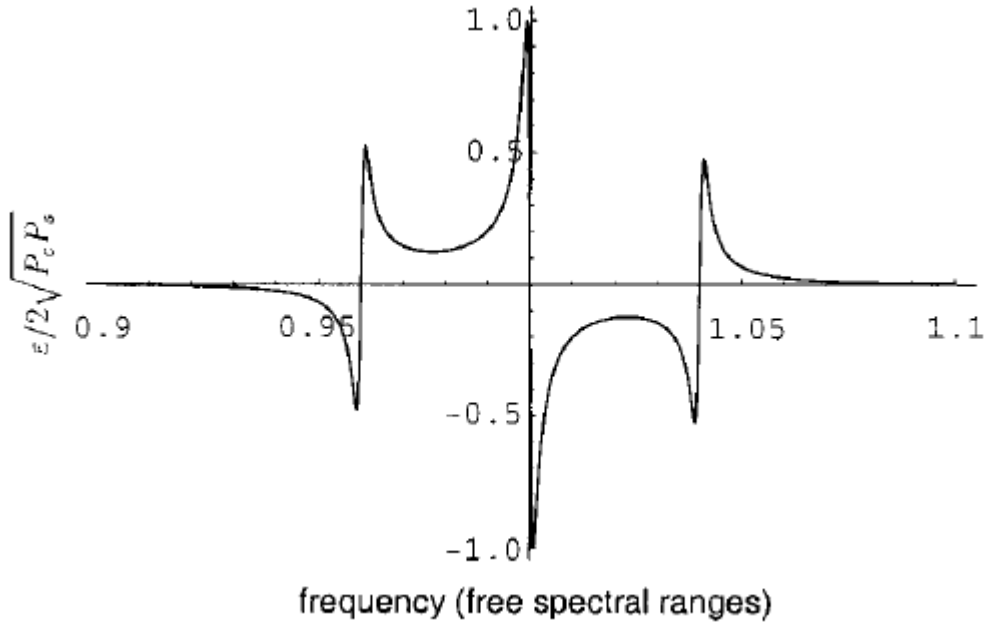


Figure 2.5: PDH error signal, in units of  $2\sqrt{P_c P_s}$ . Taken from [5].

where we used  $F(\omega)$  from Equation (2.15) and the power reflected is

$$\begin{aligned}
 P_{ref} = & P_c |F(\omega)|^2 + P_s (|F(\omega + \Omega)|^2 + |F(\omega - \Omega)|^2) \\
 & + 2\sqrt{P_c P_s} \{ \text{Re} [F(\omega)F^*(\omega + \Omega) - F^*(\omega)F(\omega - \Omega)] \cos(\Omega t) \\
 & + \text{Im} [F(\omega)F^*(\omega + \Omega) - F^*(\omega)F(\omega - \Omega)] \sin(\Omega t) \} \\
 & + (2\Omega \text{ terms})
 \end{aligned} \tag{2.24}$$

We measure this signal at the photodiode. Relevant for our analysis are only the terms in  $\cos(\Omega t)$  and  $\sin(\Omega t)$ .

Mixing two signals is mathematically equivalent to taking the product of those two signals. Thus multiplying the expression above with the local oscillator signal which is proportional to  $\sin(\Omega t)$  and using the trigonometric identity

$$\sin(a) \cdot \sin(b) = \frac{1}{2} [\cos(a - b) - \cos(a + b)], \tag{2.25}$$

we find several terms: a DC term, a term oscillating at  $\Omega$  and terms oscillating at higher frequencies. Tuning the carrier close to resonance and choosing the modulation frequency s.t. the sidebands are far-detuned from resonance then the sidebands are almost perfectly reflected. A low-pass filter then filters all oscillating terms and we are left with the so-called error signal entering the PID module (in Figure 2.4) which is

$$\epsilon = 2\sqrt{P_c P_s} \text{Im} [F(\omega)F^*(\omega + \Omega) - F^*(\omega)F(\omega - \Omega)]. \tag{2.26}$$

A plot of the error signal is visible in Figure 2.5.

Note the asymmetry of the error signal around resonance. Knowing the value of the error signal then tells us whether we are below or above resonance; a positive value corresponding to being above resonance, a negative value corresponding to being below resonance. The magnitude of the error signal additionally encodes how far away from the cavity resonance the laser frequency is. Combining these two aspects, knowledge of the error signal allows us to correct the laser frequency and bring it back to resonance. The laser frequency is thus locked to the cavity resonance frequency. If we change the cavity length then the resonance frequency will be shifted as well. Due to the constant recorection of the laser frequency to the cavity resonance, the laser frequency will shift accordingly.

### 3 Setup

#### 3.1 Optical Setup

The setup that was built as part of this project and that can be used to stabilize the 423 nm laser system is visible in Figure 3.1.

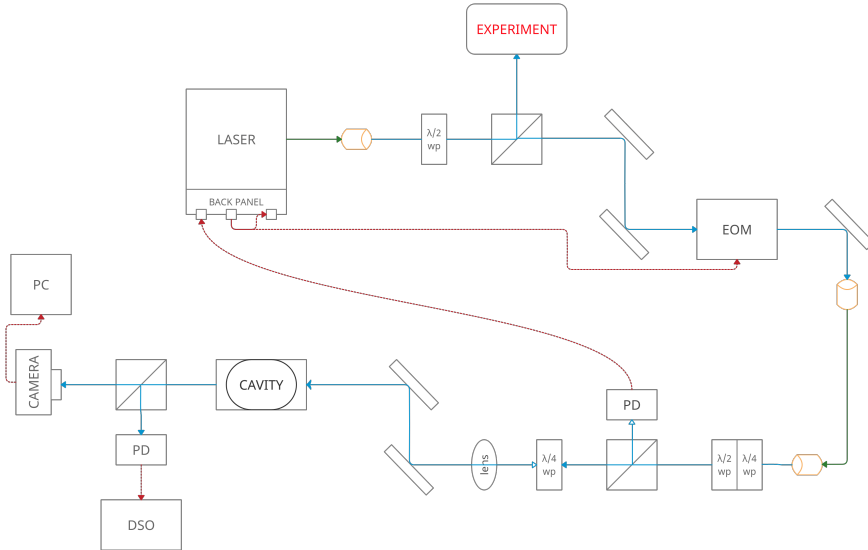


Figure 3.1: Sketch of Setup. The paths in green are optical fiber paths, the paths in blue denote free space optical paths and the paths in dashed red describe electrical paths. The orange tubes denote collimators that couple fiber modes to free space modes and vice-versa. Parts 1 and 2 as mentioned below correspond to the top and bottom part of the sketch respectively and are coupled via a fiber.

It consists of two sequential parts: In the first part, the light is modulated by an EOM, in the second part that light is fed into the cavity and the reflection that is vital for the generation of the PDH error signal is recorded.

In part 1, the laser source is coupled into an optical fiber and fed to the optical table. The light delivered by the optical fiber is fed through a waveplate into a polarizing beam splitter (PBS). The waveplate determines the polarization of the light and can be used to regulate the splitting ratio at the PBS. One of the outputs of the PBS is fed to the experiment, the other is routed into an EOM where it is modulated at 25 MHz (this is part of the PDH lock as described in Section 2.2). The system of 2 mirrors in front of the EOM aims to optimize the beam line into the EOM. The light exiting the EOM is then fed via another mirror and coupled into a collimator. The fine-adjustment on this mirror combined with the fine-adjustment on the collimator allows for optimizing the coupling efficiency.

To connect part 1 and part 2, the fiber exiting the collimator is laid around the table and out-couples into another collimator. In part 2, the light then enters a  $\lambda/4$  and  $\lambda/2$  waveplate before hitting another PBS. The system of waveplates is used to vertically polarize the light such that it is fully transmitted by the PBS. It then passes another  $\lambda/4$

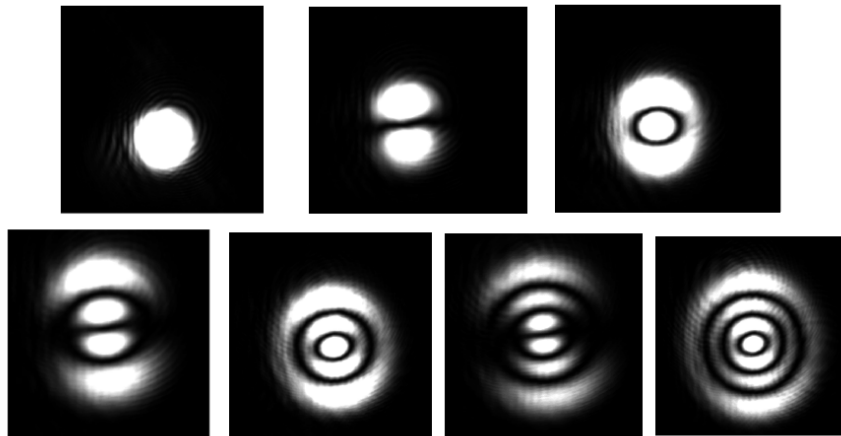


Figure 3.2: Modes as visible on the camera at the back of the cavity. The pictures are ordered from left-to-right as they appear when continuously increasing the frequency of the laser. In order:  $TEM_{00}$ ,  $TEM_{01}$ , possibly  $TEM_{02}$  (the fact that the light 'bleeds' from one element to the other might be due to oversaturation of the camera),  $TEM_{03}$ , followed by Laguerre-Gauss modes. Note that the sizes are not to scale.

waveplate that rotates the polarization from vertical to right-polarized and via a system of two mirrors enters the cavity. The mirrors are again used to optimize the beam line such that the beam is centered on the bore and perpendicular to the mirrors. A part of the light is transmitted out of the back of the cavity where it is split up with a 50:50 BS and enters a photodiode and a photcamera respectively. The photodiode records the transmission amplitude for direct observation of the lock performance and stability on an oscilloscope and the camera is used to optimize the alignment into the cavity. If the alignment is not optimal, then higher-order modes will be visible. Some pictures of modes as collected at this camera are visible in Figure 3.2. The light reflected out of the cavity and back into the aforementioned path is now left-polarized (due to the odd number of reflections at the cavity mirrors needed to exit the cavity on this side) and is rotated into horizontal polarization by the waveplate. This signal should<sup>1</sup> now be fully reflected at the PBS and enters another photodiode. This is the signal that is used for the error signal.

For some of the measurements conducted to characterize the tunable cavity additions were necessary. These are then detailed in the respective measurement section.

### 3.2 4-bore tunable cavity

We work with a custom 4-bore tunable cavity built by Stable Laser Systems in Boulder, Colorado [12]. It is visible in Figure 3.3. It consists of 4 separate tunable mirror pairs coated for use with the wavelengths 397 nm, 423 nm, 854 nm and 866 nm

<sup>1</sup>In reality, the polarization will not be perfectly vertical/horizontal and some light will be transmitted/reflected.

with finesse specified to the range 100 – 200. The cavities each contain a 0.5 inch concave/planar mirror with 50 cm ROC and a 1 inch planar/planar mirror. The former is connected to the piezo actuator, the latter is stationary. The cavity is kept under vacuum ( $\approx 10^{-7}$  mbar) by an ion pump.

The piezo actuators in the cavity are ring actuators fabricated by Noliac which are made out of a ceramic material called NCE51F [13]. The actuators are voltage controlled by a Thorlabs Piezo Controller. The free spectral range scanning voltage depends on the bore but lies between 27 and 43 V/FSR. The Thorlabs Piezo Controller in turn is voltage supplied by a custom voltage controller ('Fastino'<sup>2</sup>) which we are able to control remotely. All voltage controlled operations on the cavity are set via the Fastino. The Fastino can be set with a new desired voltage as well as a speed parameter (called 'Number of Steps'). A voltage difference of  $\Delta V_{Fast.} = 1V$  corresponds to  $\Delta V_{PC} \approx 7.5V$ , the speed parameter is treated as a relative measure and has not been independently characterized. For internal reference in the data section (Section 4) we will state these parameters whenever they are known.

In this paper we will solely focus on bore no. 3.



Figure 3.3: Picture of the 4-bore tunable cavity fabricated by Stable Laser Systems. The gray box attached to the main body of the cavity is the ion pump which keeps the cavity interior under vacuum. Bore no. 3 is located on the lower left.

---

<sup>2</sup>The Fastino is a digital-to-analog converter (DAC) board which includes a card able to receive data from a user-controlled computer. In this way, the Fastino allows for controlling voltages remotely. The operating procedure of the Fastino is described in [14].

## 4 Characterization and Interpretation

One of the goals of this project was to characterize the piezo actuators of bore 3 of the 4-bore tunable cavity. The setup that we built and that is detailed in Section 3 is used for stabilizing the 423 nm laser (denoted 423-1 internally). Note that the cavity belonging to bore 3 is coated such that it is optimal for all the transition wavelengths, not just for 423 nm, thus it could have equivalently been used for transitions at 397 nm, 855 nm or 866 nm.

In this section we describe the four different measurements we conducted to characterize the piezo actuators of bore 3. In Section 4.1 we measure the tuning range parameter, which is the parameter relating voltage differences applied to the cavity to changes in resonance frequency. In Section 4.2 we observe the settling behaviour of the cavity piezos after tuning. In Section 4.3 we characterize the hysteresis of the piezo actuators and in Section 4.4 we measure the stability of the cavity over long periods of time and determine the drift rates.

### 4.1 Tuning Range Calibration

An important quantity to know when operating the tunable cavity is the tuning range parameter. In operation we would like to tune the cavity by a certain frequency  $\Delta f$  such that the laser locked to the cavity is stabilized to some  $f_0 + \Delta f$  after the tuning. The tuning range calibration tells us the relation between the voltage that we apply - or rather the difference in voltages before and after tuning - and the change in resonance frequency.

To characterize this quantity we fed the stabilized beam (the path labelled "to experiment" in Figure 3.1) to a wavelength meter and collected a time series of the lasers frequency.<sup>3</sup> We then increased the voltage from  $V_0$  stepwise by  $\Delta V$  and measured the response. Raw time series data is visible in Figure 4.1a. In Figure 4.1b we see that the response to an increase in voltage is very well visible in the frequency data. Thus we chose to not synchronize the wavelength meter and piezo voltage controller on a hardware level but rather do the synchronization in post-processing. From the raw data in Figure 4.1a we extract  $\Delta f$  as the frequency difference between directly before and after tuning. Combined with the voltage data this leads to Figure 4.2.

From Figure 4.2 we can extract the tuning range. We fitted a first order polynomial in  $\Delta V$ , the gradient corresponds to the tuning range parameter we are interested in. We only considered data points with  $|f| < 400$  MHz. After this threshold, a significant non-linearity is visible in the data. This might be due to accumulating drifts in the piezos or

---

<sup>3</sup>In reality we placed an additional PBS in between the output of the EOM and the fiber collimator and tuned the waveplates in the path such that only a small percentage of the total beam intensity was fed to the wavelength meter. The rest was fiber coupled in a second collimator and fed to another experiment. We did so for two reasons: to protect the wavelength meter and to maximize the power going to the other experiment.

higher-order effects becoming increasingly relevant at higher voltage differences.

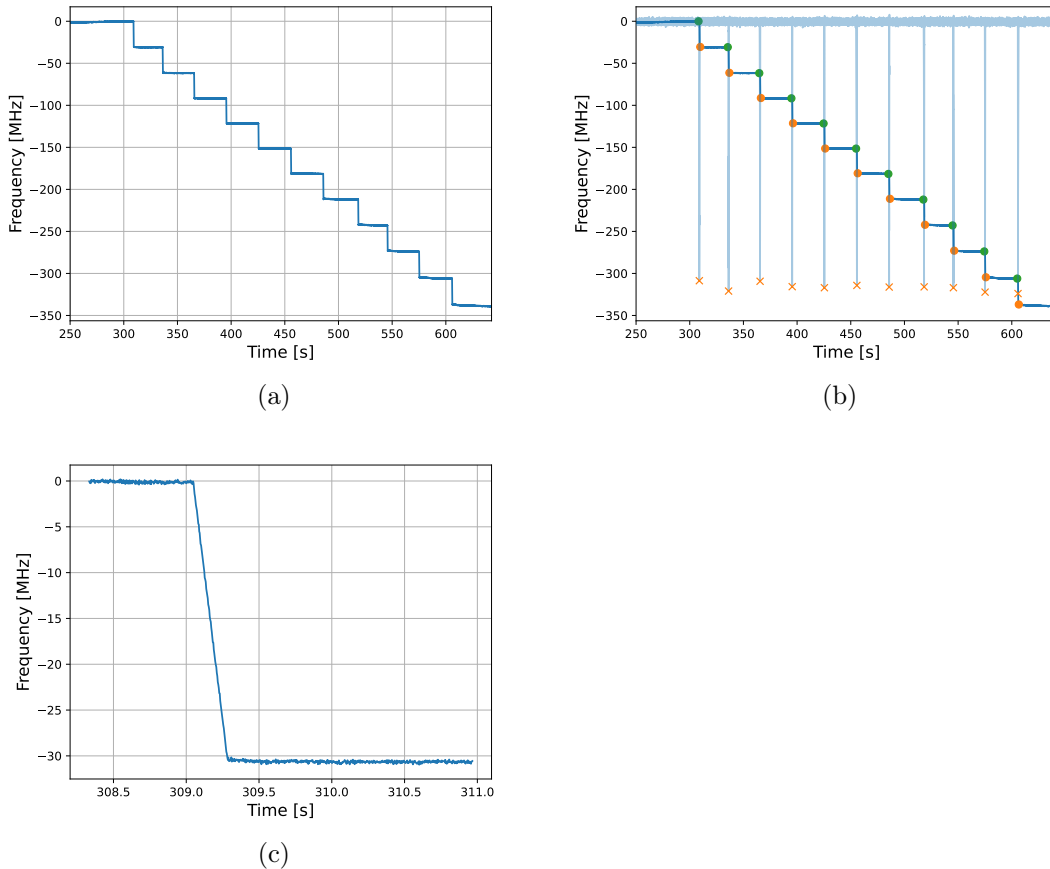


Figure 4.1: **(a)** Example raw data for the tuning range measurement. The cavity was tuned from  $V_0 = 18.64$  V to  $V_{end} = 26.77$  V with steps of  $\Delta V \approx 0.75$  V at a speed of 1200. **(b)** Example processed data from Figure 4.1a. The data in transparent blue is the derivative of the data in blue, used to determine the position of the steps. The orange and green circles were used as start and end frequency for every voltage step. We used this instead of the absolute difference between frequency after every voltage step and the initial frequency to account for drift in the piezos. **(c)** Example processed data from Figure 4.1a, zoomed into the region around  $t=300$  s. The tuning took around 200 ms to complete, the frequency of the cavity then quickly settles to a stable value. We will describe this phenomenon in more depth in Section 4.2.

We find a mean tuning range parameter of approximately  $41.0 \pm 0.35$  MHz/V for tuning starting at 18.64 V and approximately  $32.7 \pm 0.55$  MHz/V for tuning starting at 0.24 V. As visible the data for a common  $V_0$  agrees well, but there is a significant difference in the tuning range parameter for different  $V_0$ . For  $V_0 = 0.24$  V the tuning is significantly reduced compared to  $V_0 = 18.64$  V. This might indicate a non-linearity in the piezos, meaning that they are more sensitive to voltage changes at higher overall voltages. However we must note that  $V_0 = 0.24$  V is the lowest possible voltage that the Thorlabs piezo controller can supply, thus this difference in tuning might also be due to

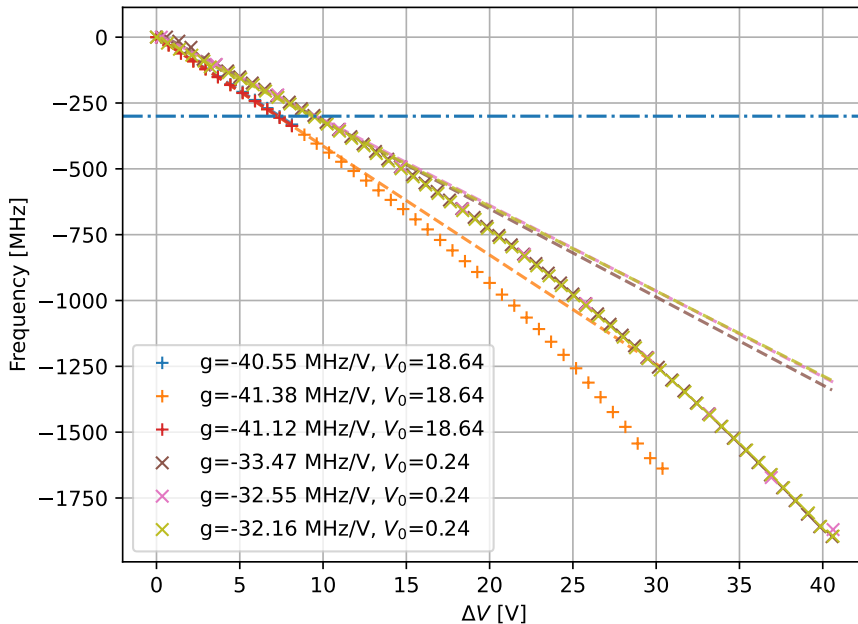


Figure 4.2: Overview of the tuning range calibration measurement. The dashed lines indicate a fit of a first order polynomial with gradient  $g$ . Cross (plus) corresponds to data taken for a  $V_0$  of 0.24 V (18.64 V). Only data points for frequencies  $|f| < 400$  MHz were considered for the fit. The blue dot-dashed line denotes a frequency of 300 MHz, which is usually the maximum value that we tune the cavity by in daily operation. The average tuning range is approximately  $41.0 \pm 0.35$  MHz/V for tuning starting at 18.64 V and approximately  $32.7 \pm 0.55$  MHz/V for tuning starting at 0.24 V.

effects caused by the Thorlabs controller independent of the piezos.

In daily operation we mostly tune the cavity by 300 MHz (indicated by the dot-dashed line in Figure 4.2) or less. Seeing that the linear fit agrees well with the data up to  $f_{th} = 400$  MHz, daily operation can be considered to be well-behaved.

## 4.2 Settling after Tuning

The goal of this particular measurement was to observe the reaction of the piezo actuators to a voltage applied to them. Specifically we aimed to observe drift in the piezo actuators in the post-actuation regime. This allows us determine a parameter regime in which stable operation is possible and tuning of the cavity results in minimum wait time. The setup of the experiment is as described in Section 3 with the addition of a waveplate followed by a polarizing beam splitter directly after the laser output. The light transmitted through the beam splitter continues as in the setup sketch shown above. The path not used for the PDH locking scheme is coupled into a fiber and fed into a wavelength meter which collects a time series of the signals wavelength. The laser is locked to the cavity and remains locked for the duration of the measurement. This allows us to directly relate the laser frequency to the distance of the two mirrors in the cavity and thus to the piezo actuators length change. At the beginning of the measurement the voltage

applied to the cavity is  $V_0$ . We start the measurement and increase the voltage linearly to a maximum of  $V_0 + V_{exc}$ .

Raw data is of the form as in Figure 4.3.

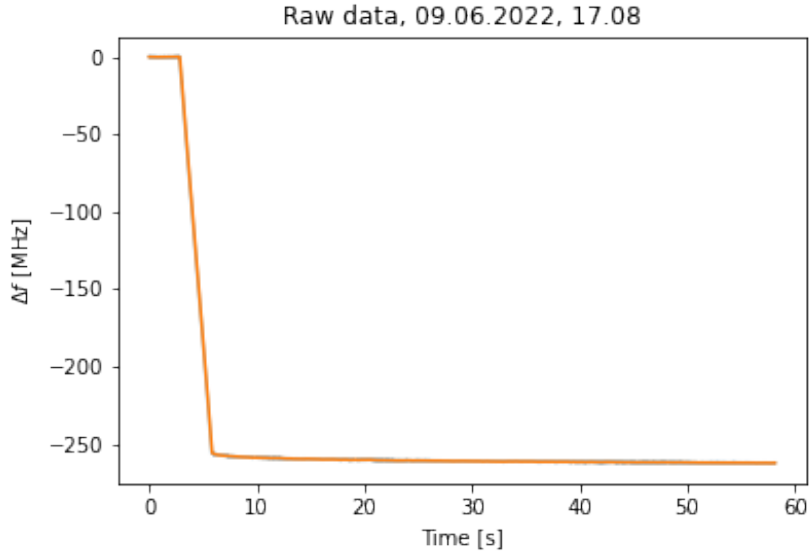


Figure 4.3: Raw data for the settling after tuning measurement. The y-axis is the frequency difference with respect to the frequency at the start of the measurement. The region with high gradient corresponds to when the voltage was continuously increased.

The region with large slope corresponds to the time in which the voltage applied to the piezo actuator was continuously increased. We focus on the subsequent region, here starting at approximately  $t = 7s$ , where the applied voltage is again constant. Cropped data is visible in Figure 4.4a for three runs with differing  $V_{exc}$ . We discern three different types of behaviour: for small  $V_{exc}$  the piezos quickly settle, for large  $V_{exc}$  they keep drifting for the duration of the measurement and for intermediate  $V_{exc}$  no clear trend is visible.

From Figure 4.4b we can then deduce for what parameter regime tuning of the piezos without continuing cavity drift is possible. We find that this is only the case for small  $V_{start}$  and  $V_{exc}$ . From the tuning range calibration in Figure 4.2 we can extract that for e.g. a displacement of 250 MHz with the cavity being under a low voltage we need to apply a voltage difference of 7.5V, which is according to Figure 4.4 lies within the region where we see significant drift. If we were to use the cavity to tune the laser frequency we would thus need to add a wait time after the tuning to allow the frequency to settle to a stable state.

Note that in the measurement we only operated in the low voltage regime  $V \in [0, 11]V$  even though the piezo controller is capable of applying up to 70V. As visible in Figure 4.4 the drift increases for increasing starting voltages, we assumed this trend to continue for voltages beyond  $V = 11 V$ . This assumption in conjunction with time constraints motivated our decision not to explore the region of higher voltages. Whether this assumption

indeed holds could be explored in further work.

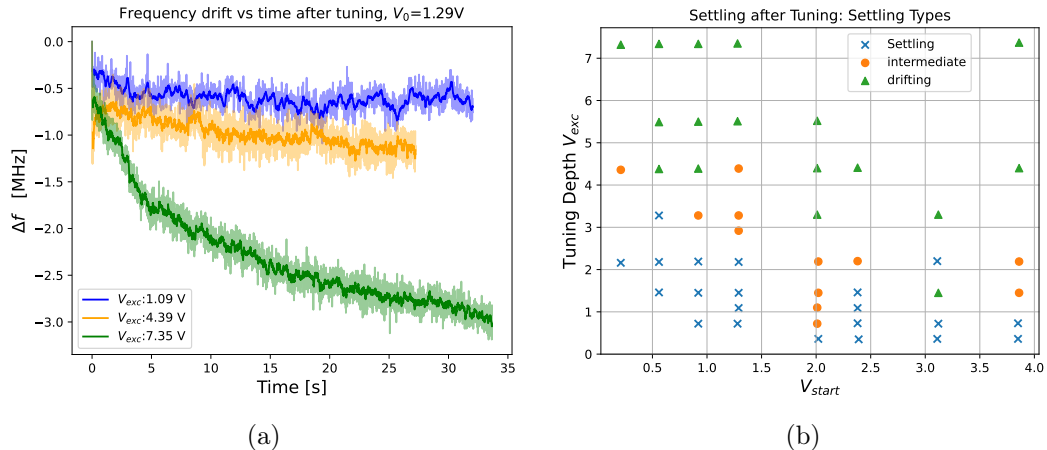


Figure 4.4: Settling dynamics after tuning: **(a)** Examples for the different behaviours observed. The top curve was classified as settling, the middle curve as intermediate, the lower curve as drifting. The x-axis denotes time (relative to the end of the voltage tuning) in seconds, the y-axis denotes the frequency relative to the frequency recorded at time  $t = 0$ . **(b)** Overview over the settling behaviour. x-axis corresponds to the voltage at which we start the tuning, y-axis the voltage amount we tune by. The speed of tuning is the same for every data point (1500 no. of steps on Fastino plugin). We differentiate three different behaviours: settling, intermediate and drifting.

### 4.3 Hysteresis

The goal of this measurement was to characterize the hysteresis of the piezo actuators in the tunable cavity.

We used the same optical setup as in Section 4.2 with the addition of a Moku Pro<sup>4</sup> virtual instrument set to function as a voltage meter. The Moku was connected to the Thorlabs Voltage Controller via a t-connector, intended to measure the voltage control signal from the Fastino plugin without impeding operation.

To explore hysteresis in the cavity piezos, we supplied them with a triangular voltage signal, ramping up from a baseline voltage  $V_0$  to some  $V_1$  and ramping down again. We collected time-series data of the laser signal stabilized to the cavity at the wavelength meter. We chose several starting voltages  $V_0$ , at every instance we ran this triangular voltage signal with three different  $V_1$  and collected the results.

Raw data is visible in Figure 4.5. The wavelength meter did not accept an external clock for clock synchronization thus we needed to synchronize the wavelength meter and Moku data in post-processing<sup>5</sup>. We then combined this raw data to plot the frequency change

<sup>4</sup>A Moku Pro is a FPGA-based virtual instrument which is capable of imitating more than 10 other instruments on one hardware platform. It can both imitate a single instrument or up to 4 instruments in series at a time. Possible instruments include an arbitrary waveform generator, an oscilloscope and a spectrum analyzer among others [15].

<sup>5</sup>We calculated the average  $m^{(0)}$  and standard deviation  $\sigma^{(0)}$  of the first 200 data points collected at the Moku. We then started iterating over all data points. At every point  $i$  we considered the lower average  $m_l^{(i)}$  (the average of the 10 data points preceding  $i$ ) and the upper average  $m_u^{(i)}$  (the average of

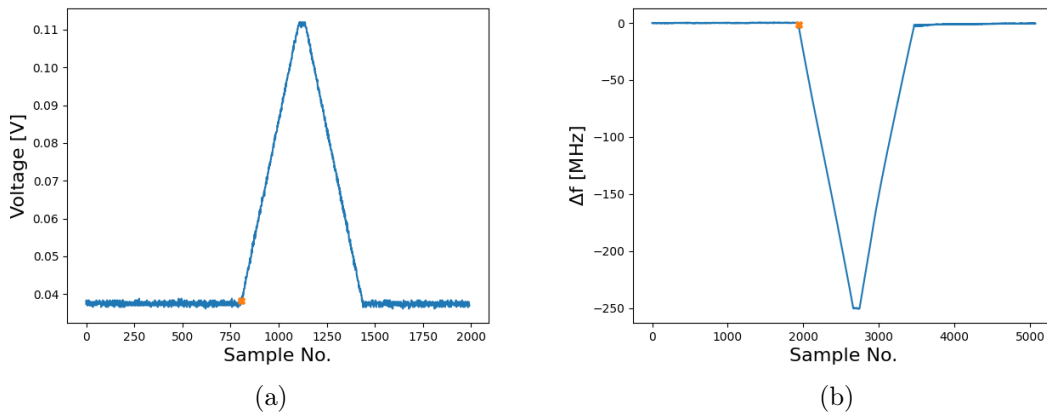


Figure 4.5: Example raw data corresponding to the measurement labelled 'Run 1' in Figure 4.6. **(a)** Example raw data of the voltage control signal as supplied by the Moku Pro. The signal was measured with an input attenuation of 40dB. The Thorlabs Piezo Controller was set to a speed of 1500. Note the orange cross marking the point of synchronization with the wavelength meter data. **(b)** Example raw data of the frequency signal as measured at the wavelength meter. Note the orange cross marking the point of synchronization with the voltage data. The y-axis is the frequency difference with respect to the start of the measurement.

with respect to the voltage signal and to achieve the familiar hysteresis cycle picture. This plot is visible in Figure 4.6.

We chose these three measurements specifically as an example as they describe the behaviour apparent in the full data well. We can see a small hysteresis in the voltage vs frequency plots for all measurement runs. The extent of the hysteresis varies slightly based on the voltage difference  $V_1 - V_0$ . It appears that for a triangular voltage signal the hysteresis almost vanishes for the parameters chosen. Thus tuning of the cavity for less than 250 MHz incurs almost no hysteresis. In real world applications a more significant constraint may be the drift described in Section 4.2.

---

the 10 data points following  $i$ ). If  $|m_l^{(i)} - m^{(0)}| < \sigma^{(0)}/2$  and  $|m_u^{(i)} - m^{(0)}| > 2 \cdot \sigma^{(0)}$ , then we considered  $i$  to be the point for synchronization. We then repeated the procedure for the wavelength meter data. This algorithm works well under the assumption that the initial data is approximately constant and that the piezos react instantaneously to a change in voltage.

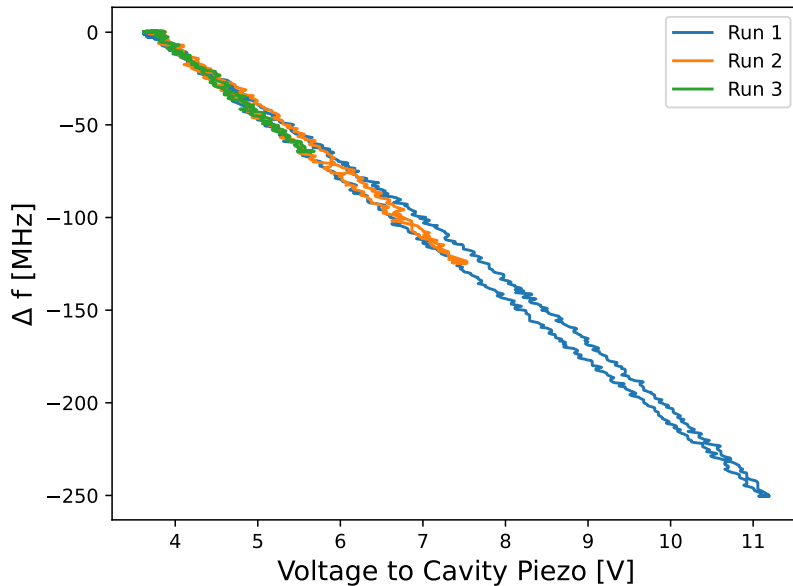


Figure 4.6: Hysteresis cycle plot. For a given starting voltage  $V_0$  we chose three different excursion voltages  $V_1$  and fed a triangular voltage signal with a maximum voltage of  $V_1$  to the Thorlabs Piezo Controller controlling the cavity. Simultaneously we collected the laser frequency stabilized to the cavity at the wavelength meter. Raw data used to create this plot can be found in Figure 4.5.

#### 4.4 Longterm Drift

We acknowledge data collection and large contributions to the construction of this setup by Olivia Hefti <sup>6</sup>.

The goal of this measurement was to observe the stability of the cavity over long timespans and to characterize drift rates.

We used the same setup as in Section 4.2. The 423 laser was locked to the cavity at a frequency of approximately  $f = 709.08416$  THz, the path labelled 'to experiment' was fed to the wavelength meter. The wavelength meter was set to recalibrate itself to its He-Ne reference every 10 minutes. We measured the wavelength every 10 s to both reduce the amount of data and suppress high-frequency fluctuations. A measurement rate of 0.1 Hz should allow us to identify fluctuations at frequencies up to 0.05 Hz. The wavelength meter is also capable of recording the temperature and pressure of the room at its location which we additionally collected. The resulting data is visible in Figure 4.7.

In the overview plot in Figure 4.7 we note a stronger drift from  $t = 0$  h to  $t = 10$  h and subsequent better stabilization. The sign of the drift changes at around  $t = 10$  h which correlates with a sign change in the temperature at the wavelength meter. The remaining evolution of the drift can however not be satisfactorily explained by considering the temperature and pressure at the wavelength meter only, as for example the evolutions

<sup>6</sup>olivia.hefti@csem.ch

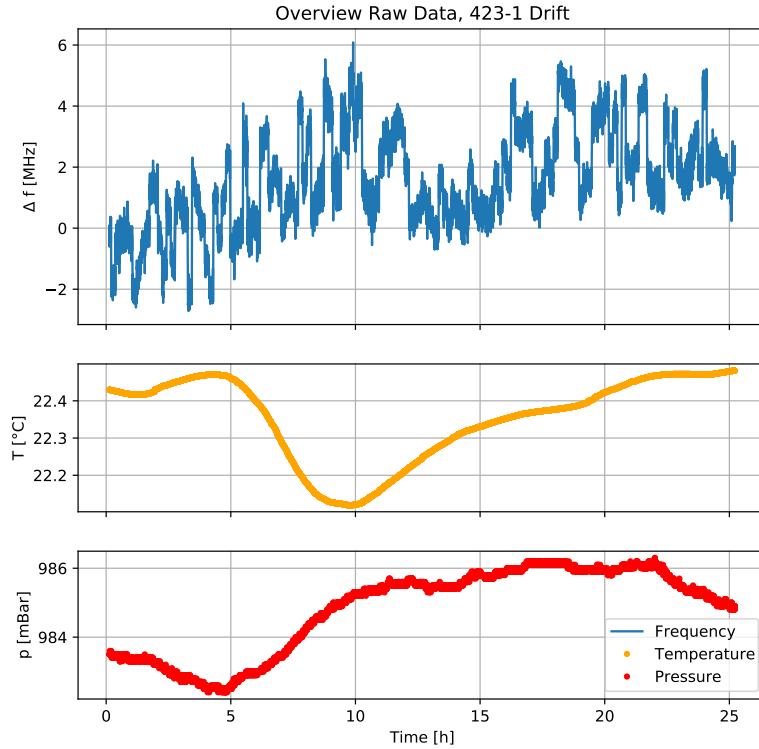


Figure 4.7: Overview of collected data points for the 423 nm drift measurement. Top displays the fluctuations in laser frequency, middle temperature fluctuations, bottom the pressure fluctuations. Note the sign change in drift direction at around 10h.

of drift and temperature do not correlate well. From this we conclude that the grand evolution of the drift is not due to some time-dependent changes in the measurement apparatus. Instead we now want to consider the temperature around the cavity, which is best described by the lab temperature as recorded by the lab monitoring system. This data is visible in Figure 4.8.

We see that over the full measurement duration of 25 h, the temperature variation is at maximum 0.6 C. The temperature is fairly stable up to  $t = 5$  h, drops to its minimum at  $t \approx 6.5$  h and rises slowly for the remainder of the measurement, levelling off at  $t \approx 10$  h. This behaviour correlates with the average evolution of the drift as the average frequency as well is fairly stable for the first 5 h, rises between  $t = 5$  h and  $t = 10$  h and after a sharp decline at  $t = 10$  h settles to a slower rise for the duration of the measurement.

To conserve readability of the plot we chose to display the time series data with a continuous line. Note however that the data consists of many rapid 'jumps' as is visualized in Figure 4.9 where we zoom in on a time window spanning 2.5 h centered around  $t \approx 15.5$  h. Thus we find that the drift can be separated as such: slow drift on a timescale much larger than our temporal resolution, which is well correlated with temperature, and fast

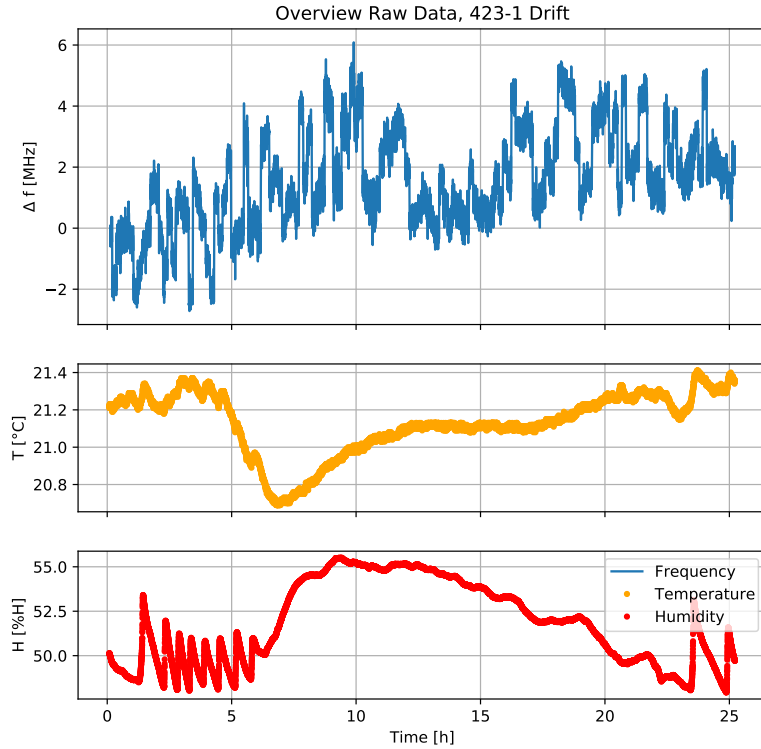


Figure 4.8: Overview of collected data points for the 423 nm drift measurement, now compared to the *lab* temperature (instead of the wavelength meter temperature as in Figure 4.7) and humidity.

jumps on a timescale smaller than our temporal resolution.

The jumps in frequency occur with a period of approximately 615 s (10 minutes and 15 s). Considering both the fact that the wavelength meter recalibrates itself to its He-Ne reference every 10 minutes and its precision of 400 kHz, the jumps may be caused by this recalibration. The jumps might also be due to suboptimal performance of the lock, in that case they could be reduced by optimising the locking parameters.

Directly fitting a linear regression to the drift time series we find the drift rates. We distinguish the average and the worst case, the latter being the drift rate between  $t = 0$  h and  $t = 10$  h. The fits are visible in Figure 4.10, we find a worst case drift rate of  $\Gamma_{wc} \approx 400$  kHz/h and a average drift rate of  $\Gamma_{av} \approx 140$  kHz/h.

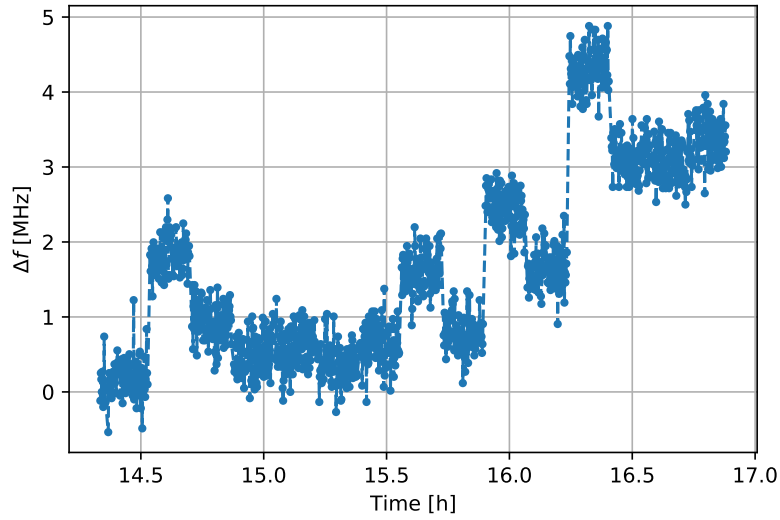


Figure 4.9: 423 nm Drift Measurement, zoomed in on a window spanning 2.5 h centered around  $t \approx 15.5$  h. Data is marked by blue dots and interpolated with a dashed line. The areas where the dashed line is clearly visible are where we find large rapid jumps in frequency (meaning occuring on a timescale smaller than our temporal resolution of  $\Delta t \approx 7$  s.)

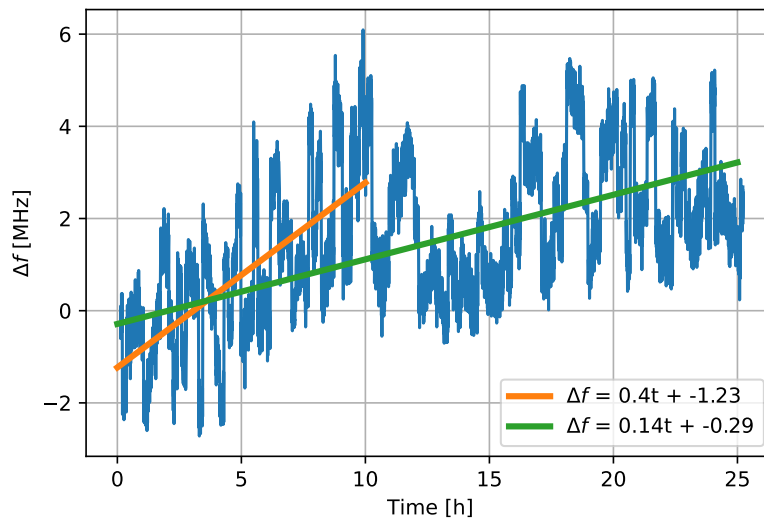


Figure 4.10: Longterm drift measurement from which we extract the drift rates. Measurement data is depicted in blue, worst case drift rate in orange and average drift rate in green. We find a worst case drift rate of  $\Gamma_{wc} \approx 400$  kHz/h and a average drift rate of  $\Gamma_{av} \approx 140$  kHz/h.

## 5 Summary and Outlook

In this paper we described the setup and characterization of a tunable cavity. We gave a brief introduction to cavity theory and Pound-Drever-Hall locking and described the setup necessary to implement the PDH locking scheme. We characterized one of the 4 bores of our 4-bore tunable cavity and analyzed the response of the built-in piezo actuators. Specifically we conducted four measurements: a tuning range calibration to relate voltage differences to frequency differences, a settling measurement to determine the amount of drift in the piezos after actuation, a hysteresis cycle measurement and a longterm drift measurement. We found that the tuning range calibration parameter depends on the starting voltage but lies between 33 and 40 MHz/V. The drift after tuning divides into three categories for different excursion voltages: for low start and excursion voltages the piezos quickly settle to a steady state, for large start and excursion voltages they keep drifting indefinitely and for intermediate parameters the trend lies between the two described before. The hysteresis measurement showed that there is a small hysteresis present in the piezos that depends weakly on the voltage difference. The longterm drift measurement led us to the conclusion that the drift is a superposition of two distinct phenomena: jumps on a timescale smaller than our temporal resolution and slow drift on a larger timescale. We determined the drift rates to be 140 kHz/h in the average case and up to 400 kHz/h in the worst case scenario.

In future work, we could investigate the source of the rapid jumps visible in the longterm drift data such that their impact on the drift rate could be mitigated. Reducing or eliminating them could lead to a significant improvement in the drift rate. One way of achieving this goal would be to repeat the measurement with a different instrument measuring the wavelength, such as a frequency counter attached to a photodiode. Additionally we could repeat the settling measurement for higher starting voltages to determine whether there are other parameter sets that allow for quick operation without large drifts after tuning.

## 6 Acknowledgements

I would like to thank Cornelius Hempel for giving me the opportunity of writing this semester thesis in his group and Prof. Home for officially supervising it. Additionally I would like to thank Flavia Timpu and Jackson Ang'ong'a for their excellent hands-on supervision and comments in the writing of this report. Finally a big thank you also goes to Olivia Hefti for the help in building the setup and collecting the data.

## References

- [1] OZERI, Roee: The trapped-ion qubit tool box. In: *Contemporary Physics* 52 (2011), Nov, Nr. 6, 531–550. <http://dx.doi.org/10.1080/00107514.2011.603578>. – DOI 10.1080/00107514.2011.603578
- [2] ZHU, Shi-Liang ; MONROE, C. ; DUAN, L.-M.: Trapped Ion Quantum Computation with Transverse Phonon Modes. In: *Phys. Rev. Lett.* 97 (2006), Aug, 050505. <http://dx.doi.org/10.1103/PhysRevLett.97.050505>. – DOI 10.1103/PhysRevLett.97.050505
- [3] KIELPINSKI, David ; MONROE, Christopher R. ; WINELAND, David J.: Architecture for a large-scale ion-trap quantum computer. In: *Nature* 417 (2002), S. 709–711
- [4] KIENZLER, Daniel: *Trapped-ion physics lecture*. March 2022. – Lecture Notes for Trapped Ion Physics Lecture
- [5] BLACK, Eric D.: An introduction to Pound-Drever-Hall laser frequency stabilization. In: *American Journal of Physics* 69 (2001), S. 79–87
- [6] SIEGMAN, A.E.: *Lasers*. University Science Books, 1986 <https://books.google.ch/books?id=1BZVwUZLTkAC>. – ISBN 9780935702118
- [7] MARINELLI, Matteo: *High finesse cavity for optical trapping of ions*. 2014
- [8] KIRCHMAIR, Gerhard: Frequency stabilization of a Titanium-Sapphire laser for precision spectroscopy on Calcium ions, 2006
- [9] DREVER, Ronald W. P. ; HALL, John L. ; KOWALSKI, Frank V. ; HOUGH, James ; FORD, G. M. ; MUNLEY, A. J. ; WARD, H.: Laser phase and frequency stabilization using an optical resonator. In: *Applied Physics B* 31 (1983), S. 97–105
- [10] BLACK, Eric: Notes on the Pound Drever Hall technique. – Technical Note, LIGO Project
- [11] LINDENFELSER, Frieder: *Laser stabilisation for quantum information experiments with trapped ions*. 2011
- [12] SYSTEMS, Stable L.: *Stable Laser Systems*. <https://stablelasers.com/>. – "Accessed: 28.07.2022"
- [13] NOLIAC: *NAC2123*. <http://www.noliac.com/products/actuators/ring-actuators/show/nac2123/>. – "Accessed: 31.07.2022"
- [14] MARTI, Michael: *Low-Noise DC Amplifier Design for Trapped Ion Setups & Bayesian Schemes for Fast Single Qubit Detection*. 2022
- [15] MOKU: *Moku Pro*. <https://www.liquidinstruments.com/products/hardware-platforms/mokupro/>. – "Accessed: 14.10.2022"

**Eigenständigkeitserklärung**

Die unterzeichnete Eigenständigkeitserklärung ist Bestandteil jeder während des Studiums verfassten Semester-, Bachelor- und Master-Arbeit oder anderen Abschlussarbeit (auch der jeweils elektronischen Version).

Die Dozentinnen und Dozenten können auch für andere bei ihnen verfasste schriftliche Arbeiten eine Eigenständigkeitserklärung verlangen.

Ich bestätige, die vorliegende Arbeit selbständig und in eigenen Worten verfasst zu haben. Davon ausgenommen sind sprachliche und inhaltliche Korrekturvorschläge durch die Betreuer und Betreuerinnen der Arbeit.

**Titel der Arbeit** (in Druckschrift):

Setup and Characterization of a 4-bore tunable cavity

**Verfasst von** (in Druckschrift):

*Bei Gruppenarbeiten sind die Namen aller Verfasserinnen und Verfasser erforderlich.*

**Name(n):**

Corminboeuf

**Vorname(n):**

Etienne

Ich bestätige mit meiner Unterschrift:

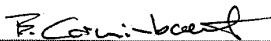
- Ich habe keine im Merkblatt „Zitier-Knigge“ beschriebene Form des Plagiats begangen.
- Ich habe alle Methoden, Daten und Arbeitsabläufe wahrheitsgetreu dokumentiert.
- Ich habe keine Daten manipuliert.
- Ich habe alle Personen erwähnt, welche die Arbeit wesentlich unterstützt haben.

Ich nehme zur Kenntnis, dass die Arbeit mit elektronischen Hilfsmitteln auf Plagiate überprüft werden kann.

**Ort, Datum**

Zürich, 29.11.2022

**Unterschrift(en)**



*Bei Gruppenarbeiten sind die Namen aller Verfasserinnen und Verfasser erforderlich. Durch die Unterschriften bürgen sie gemeinsam für den gesamten Inhalt dieser schriftlichen Arbeit.*